Inorganic Chemistry

pubs.acs.org/IC

Article

Tuning the Morphology and Electronic Properties of Single-Crystal $LiNi_{0.5}Mn_{1.5}O_{4-\delta}$: Exploring the Influence of LiCl–KCl Molten Salt Flux Composition and Synthesis Temperature

Stephanie L. Spence, Zhengrui Xu, Sami Sainio, Dennis Nordlund, and Feng Lin*

Cite This: https://dx.doi.org/10.1021/acs.inorgchem.0c01042

Read Online

ACCESS | Metrics & More | Article Recommendations | Supporting Information

ABSTRACT: Single-crystal materials have played a unique role in the development of high-performance cathode materials for Li batteries due to their favorable chemomechanical stability. The molten salt synthesis method has become one of the most prominent techniques used to synthesize single-crystal layered and spinel materials. In this work, the molten salt synthesis method is used as a technique to tune both the morphology and Mn^{3+} content of high-voltage $LiNi_{0.5}Mn_{1.5}O_4$ (LNMO) cathodes. The resulting materials are thoroughly characterized by a suite of analytical techniques, including synchrotron X-ray core-level spectroscopy, which are sensitive to the material properties on multiple length scales. The multidimensional characterization allows us to build a materials library according to the molten salt phase diagram as well as to establish the relationship among synthesis, material properties, and battery performance. The results of this work show that the Mn^{3+} content is primarily dependent on the synthesis temperature and increases as the temperature is increased. The particle morphology is mostly dependent on the composition of the molten salt flux, which can be tailored to obtain well-defined octahedrons enclosed by (111) facets, plates with predominant $(11\bar{2})$ facets, irregularly shaped particles, or mixtures of these. The electrochemical measurements indicate that the Mn^{3+} content has a larger contribution to the battery performance of LNMO than do morphological characteristics and that a significant amount of Mn^{3+} could become detrimental to the battery performance. However, with similar Mn^{3+} contents, morphology still plays a role in influencing the battery cycle life and rate performance. The insights of molten salt synthesis parameters on the formation of LNMO, with deconvolution of the roles of Mn^{3+} and morphology, are crucial to continuing studies in the rational design of LNMO cathode materials for high-energy Li batteries.

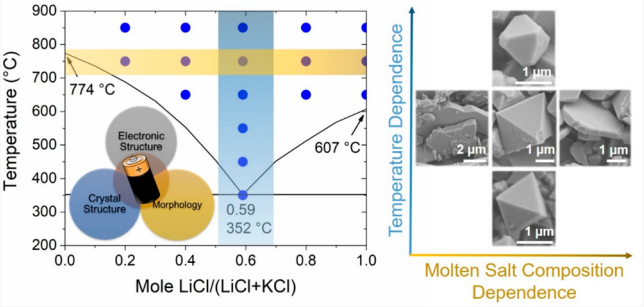

1. INTRODUCTION

Today, lithium ion batteries are ubiquitous in consumer electronics such as laptops and cellular devices due to their high energy density and cycling performance.[1] However, further improvements in safety, energy density, and cycle life are necessary to meet the increasing demands of additional large-scale applications, such as electric vehicles.[2] High-voltage cathode materials have been investigated as possible strategies to meet these requirements. Of these, spinel $LiNi_{0.5}Mn_{1.5}O_4$ (LNMO) is one of the most promising cathode materials for lithium batteries due to its high working potential (4.7–4.9 V vs Li/Li^+), reasonable theoretical capacity (148 mAh/g), high energy density (650 Wh/kg), abundance of raw materials, and three-dimensional lithium diffusion paths leading to a high rate capability.[3−5] In addition to being the most attractive feature of this material, a high operating voltage can also lead to electrolyte degradation and capacity deterioration, especially at elevated temperatures, which has been a barrier to the practical application of LNMOs.[6] Fluorinated solvents such as fluoroethylene carbonate (FEC) or salt additives such as lithium bis(oxalate)borate (LiBOB) and dimethyl methylphosphonate (DMMP) have been used to improve the cycling performance compared to traditional electrolytes composed of $LiPF_6$ salt dissolved in carbonates.[7] Furthermore, the development of solid electrolytes with high lithium ion conductivity and stable interfaces may also solve the intrinsic issues related to high voltage operation batteries including those using LNMO.

In spinel LNMO, oxygen adopts a cubic-close-packed array with lithium ions occupying the tetrahedral sites and transition metals in the octahedral sites. Depending on the synthesis conditions, LNMO adopts two different crystal structures.[8] An ordered phase of space group $P4_332$ is formed when Ni and Mn ions occupy 4a and 12b Wyckoff positions, respectively.[9]

Received: April 8, 2020

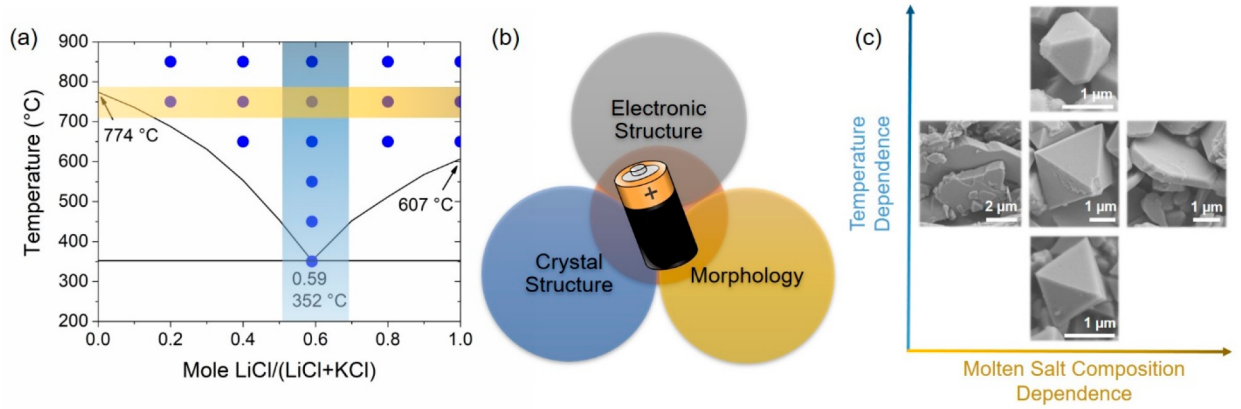

Figure 1. (a) LiCl−KCl phase diagram illustrating tunable synthesis parameters. (b) Material properties influencing electrochemical performance, which are studied in the work. (c) Selected SEM images to illustrate temperature-dependent and molten salt composition-dependent particle morphologies. Note that the particle sizes are not representative.

This stoichiometric material has Ni^{2+} and Mn^{4+} fixed oxidation states. With high-temperature calcinations (>700 °C), a disordered $Fd\bar{3}m$ phase can be formed with Ni and Mn randomly distributed on the 16d sites.[8] In the disordered phase, nonstoichiometric LNMO can be accompanied by the presence of oxygen vacancies and/or Mn^{3+}.[10,11] The oxygen-deficient material is often expressed as $LiNi_{0.5}Mn_{1.5}O_{4-\delta}$. An additional voltage plateau appears at ∼4.0 V due to the electrochemically active Mn^{3+}, which is believed to improve the performance through increased electronic conductivity and Li^+ diffusion.[12,13] However, the presence of Mn^{3+} may also lead to Jahn−Teller distortion and transition-metal dissolution via the disproportionation reaction ($2Mn^{3+} \rightarrow Mn^{2+} + Mn^{4+}$), which can lead to capacity fading.[14] The formation of the disordered phase is also closely associated with the formation of rock-salt $Li_xNi_{1-x}O$-type impurities due to the high-temperature synthesis conditions.[5] $Fd\bar{3}m$ LNMO can be transformed to $P4_332$ with postsynthesis annealing near 700 °C, followed by slow cooling, which can restore oxygen to the lattice.[8,11,15]

Much research focus on LNMO has been on correlating material properties such as the particle size and morphology, crystal structure, and Mn^{3+} content to electrochemical performance.[16−20] It is necessary to understand how experimental conditions can affect the degree of cation ordering and Mn oxidation state in LNMO for the rational design of high-voltage cathode materials. While efforts to decouple and individually study the properties of LNMO have been undertaken,[21−24] the significance of morphology versus structural ordering or Mn^{3+} content as the dominant feature in dictating performance has been debated due to the difficulty of studying each parameter in isolation. Molten salt synthesis techniques, utilizing a low-melting-point salt or a mixture of salts as a reaction medium, has been used as an effective method to precisely control the properties of LNMO.[25−27] The low-melting-point flux allows for increased diffusion of the reactants, improving the crystallinity of the final product. The particle size and morphology and the extent of order/disorder and Mn^{3+} content can all be tuned through varying synthesis conditions including temperature, heating duration, precursors, molten salts, and ratios of reactants and salts.[8,25,28] Kim et al. have studied the effect of the calcination atmosphere, amount of molten salt, synthesis temperature, and synthesis time on the formation of LNMO via molten salt synthesis.[25] Furthermore, Hai et al. have prepared octahedral and plate-like LNMO differing in Mn^{3+} content using eutectic LiCl−KCl and pure LiCl fluxes, respectively.[28] However, to the best of our knowledge, the influence of both the LiCl−KCl flux composition and synthesis temperature on LNMO formation has not yet been thoroughly studied, particularly in terms of the interrelationship among molten salt composition, temperature, crystal structure, electronic properties, morphology, and battery performance.

Herein, we have prepared a series of LNMO materials via a molten LiCl−KCl salt synthesis method. Through systematically varying the maximum synthesis temperature and the composition of the salt flux across the phase diagram from 20 to 100% LiCl (Figure 1), we can tune the melting point of the composite salt mixture, affecting the conditions of particle formation. We correlate how the synthesis parameters of the molten salt method affect the morphology, size, crystal structure, and electronic properties (including Mn^{3+} and oxygen deficiencies) and, in-turn, how these material characteristics affect the electrochemical performance of LNMO cathodes. This study provides a platform for studying the molten salt synthesis-dependent material characteristics to inform the future rational design of LNMO cathode materials.

2. EXPERIMENTAL SECTION

2.1. Sample Preparation. Stoichiometric amounts of $Ni(NO_3)_2 \cdot 6H_2O$ (Sigma-Aldrich) and $Mn(NO_3)_2 \cdot 4H_2O$ (Sigma-Aldrich) (1:3) were dissolved in a minimum amount of deionized water. LiCl (Ward's Science) and KCl (Alfa Aesar) were added in a molar ratio of 1:30 transition metals (TM)/salts. The ratio of LiCl to KCl was varied. The mixture was ground in a mortar and then heated in a 40 mL uncovered porcelain crucible housed in a box furnace in an air environment at a ramp rate of 2 °C/min, holding for 8 h at the maximum desired temperature. The resultant powders were thoroughly washed with deionized water and isopropyl alcohol to remove any salt residue and then dried in a vacuum oven at 80 °C overnight to obtain approximately 1 g of LNMO. Approximately 4% of the salt flux was lost to evaporation during heating. The low synthesis temperatures resulted in minimal evaporation, while the high TM/salt ratio makes this loss negligible in terms of the reaction media.

2.2. Materials Characterization. X-ray diffraction (XRD) patterns were acquired using a benchtop Rigaku Miniflex II with a Cu Kα light source (λ = 1.54 Å). Patterns were collected from 10−80° 2θ with a step size of 0.02° 2θ and a 1.0 s count time. Fullprof software was used for structural refinement using the Rietveld

https://dx.doi.org/10.1021/acs.inorgchem.0c01042
Inorg. Chem. XXXX, XXX, XXX−XXX

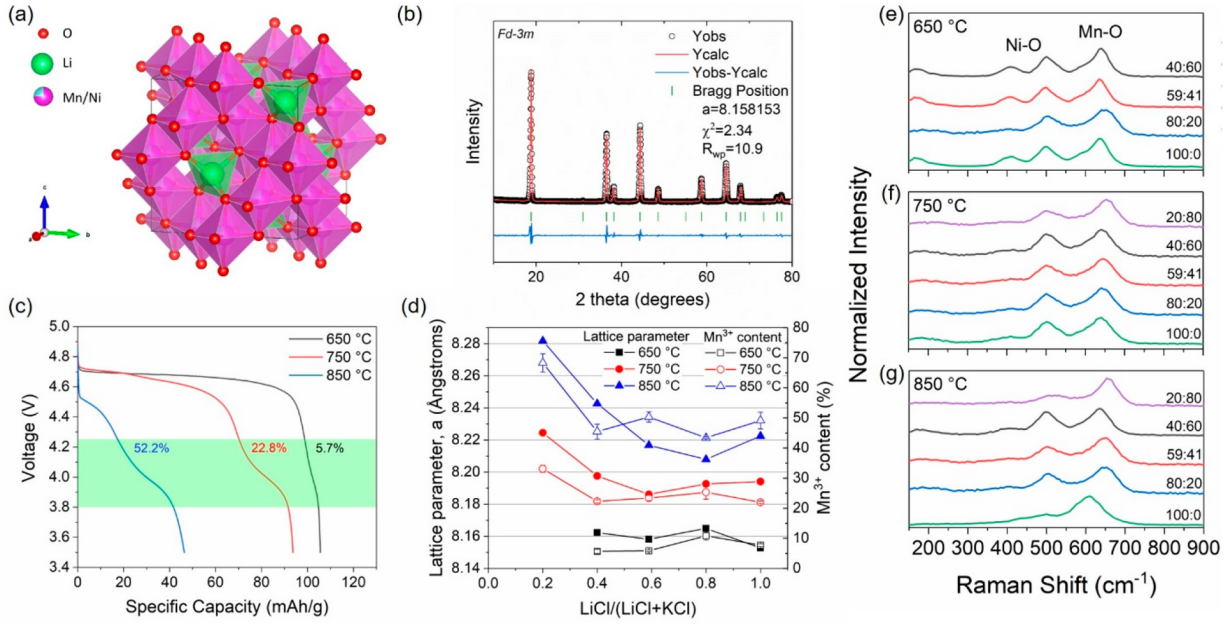

Figure 2. (a) Crystal structure of $Fd\bar{3}m$ LNMO. (b) XRD pattern and Rietveld refinement of LNMO synthesized using eutectic LiCl−KCl at 650 °C. (c) Discharge profiles of LNMO synthesized using eutectic LiCl−KCl at 0.1 C to illustrate that the increase in synthesis temperature increases the capacity contribution in the 3.8−4.25 V region due to the Mn redox. (d) Comparison of lattice parameters calculated by Rietveld refinement and approximate Mn^{3+} contents to illustrate the similarity of trends as the synthesis temperature and molten salt composition are varied. (e−g) Raman spectra of LNMO prepared with different LiCl−KCl compositions at 650, 750, and 850 °C, where the ratios represent the molar ratio LiCl−KCl.

method. Soft X-ray absorption spectroscopy (XAS) was performed on 31-pole wiggler beamline 10-1 at Stanford Synchrotron Radiation Lightsource (SSRL). A ring current of 350 mA and a 1000 L/mm spherical grating monochromator with a 20 μm entrance and exit slit were used to acquire ~10^{11} ph/s at a 0.28 eV resolution in a 1 mm^2 beam spot. Data was collected under ultrahigh vacuum (10^{-9} Torr) in a single load at room temperature. Spectra were normalized by the current from freshly evaporated gold on a fine grid positioned upstream from the main chamber. Raman spectra were collected on a WITec Raman spectrometer with a 633 nm laser beam. Scanning electron microscopy (SEM) was used to investigate the particle morphology using an LEO FESEM at an acceleration voltage of 5.0 kV.

2.3. Electrochemical Measurements. Electrodes were prepared by mixing 80 wt % LNMO active material, 10 wt % polyvinylidene fluoride (PVdF) binder, and 10 wt % carbon black conductive additive in *N*-methyl-2-pyrrolidone (NMP). The slurries were cast on carbon-coated aluminum foils using a doctor blade. Cathode disks with an area of 0.785 cm^2 were cut from the electrode sheets and dried in a vacuum oven at 120 °C overnight before being transferred to an argon-filled glovebox. Coin cells were assembled using CR2032 coin cell parts with Li foils as the anode and Celgard 2400 polypropylene membranes as the separators. The electrolyte was 1 M $LiPF_6$ in 3:7 v/v ethylene carbonate (EC)/dimethyl carbonate (DMC). Electrochemical measurements were carried out on a LAND battery testing system from 3.5 to 4.9 V vs Li/Li^+. For galvanostatic charge/discharge experiments, cells were cycled at 0.1 C (1 C = 148 mAh/g). For rate capability testing, cells were cycled three times at 0.1 C and then charged at 0.1 C and discharged at different current densities.

3. RESULTS AND DISCUSSION

3.1. Influence of Molten Salt Composition and Synthesis Temperature on the Crystal Structure and Mn^{3+} Content. LNMO was synthesized using the molten salt method with different compositions of LiCl and KCl to span the phase diagram of the two salts. LiCl−KCl compositions of 100:0, 80:20, 59:41, and 40:60 were used as reaction mediums, and each composition was used to synthesize materials at maximum temperatures of 650, 750, and 850 °C. A ratio of 20:80 LiCl/KCl was used to synthesize materials only at 750 and 850 °C due to the high composite melting temperature of 688 °C;[29] synthesis at 650 °C would lead to incomplete melting of the salts. The ratio of 59:41 LiCl/KCl represents the eutectic composition of LiCl and KCl in which the mixture has a minimum melting temperature of 352 °C. In order to investigate the cation ordering and Mn reduction induced through varying synthesis parameters, no additional postsynthesis annealing was performed. Figure 1 shows the synthesis points of interest along the LiCl−KCl phase diagram as well as the material properties considered to be factors dictating electrochemical performance. Selected SEM images are also shown in Figure 1 to summarize the changes in particle morphology as a function of synthesis conditions.

To first investigate the crystal structure of the synthesized materials, powder XRD patterns were collected (Figure S1). All 14 materials of interest were indexed to the cubic $Fd\bar{3}m$ space group. A small amount of impurity phases was found to increase with the synthesis temperature. The presence of electrochemically inactive rock-salt $Li_xNi_{1-x}O$-type impurities occurs with synthesis temperatures above 700 °C, where they become thermodynamically stabilized.[30] The crystal structure model for this space group is presented in Figure 2a, which shows that Ni and Mn cations are randomly arranged in the octahedral sites of the face-centered-cubic framework. Additional subphases such as spinel $LiMn_2O_4$ may also be present in nontrivial amounts in highly disordered samples with increased $Li_xNi_{1-x}O$ impurities due to the segregation of Ni and Mn.

Rietveld refinement was performed on the basis of a single $Fd\bar{3}m$ phase model to determine the lattice parameter, *a*, for

https://dx.doi.org/10.1021/acs.inorgchem.0c01042
Inorg. Chem. XXXX, XXX, XXX−XXX

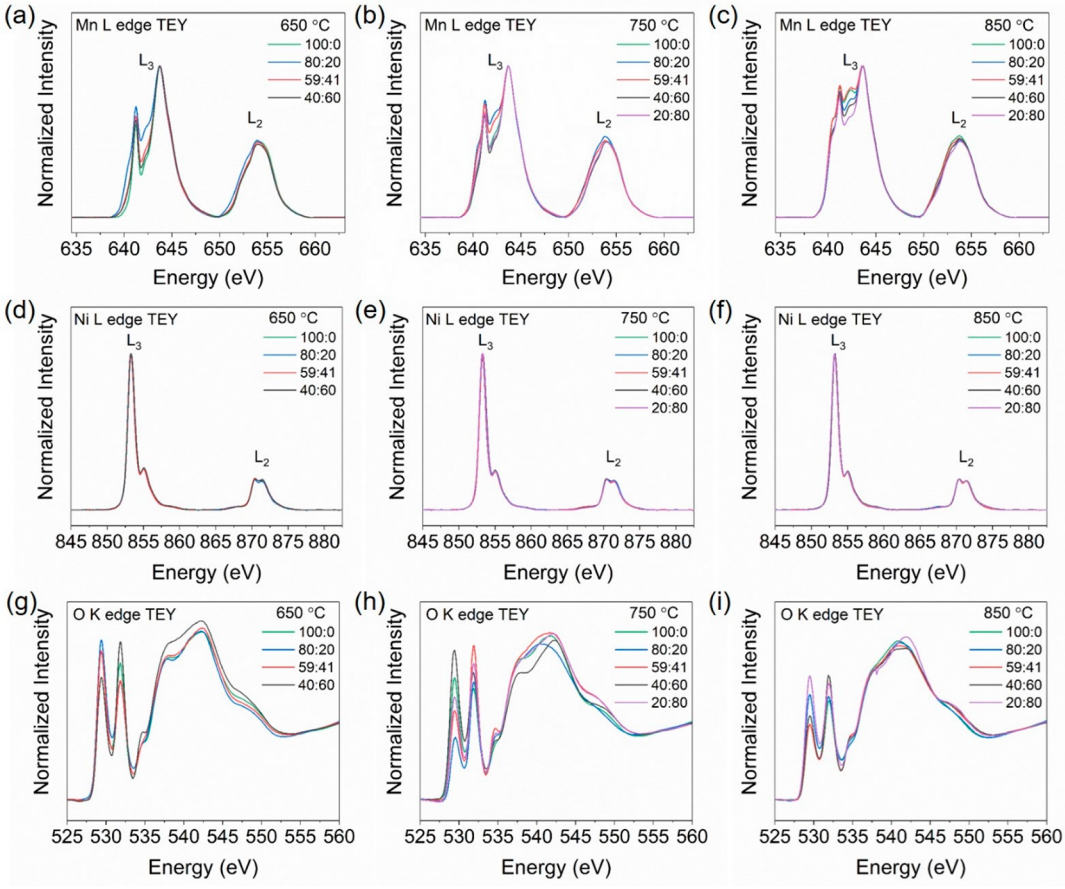

Figure 3. Soft XAS spectra of LNMO prepared with various LiCl−KCl compositions at fixed temperatures of (a) 650, (b) 750, and (c) 850 °C in the TEY collection mode. Mn L-edges illustrating Mn reduction at higher synthesis temperatures and variation of the Mn oxidation state with various salt ratios at fixed synthesis temperatures. (d−f) Ni L-edges illustrating a constant oxidation state and (g−i) O K-edges illustrating decreased TM−O hybridization at higher synthesis temperatures and variation of the TM−O hybridization with various salt ratios at fixed synthesis temperatures.

each sample (Figure 2b). The full table of structural parameters obtained from the refinement analysis is displayed in Supporting Information Table S1. Figure 2c shows the discharge profiles for the materials synthesized using the eutectic salt ratio at each temperature. The plateau at ∼4.0 V originates from the Mn^{3+}/Mn^{4+} redox.[8] The Mn^{3+} content from each sample was approximated from the discharge profile by determining the percent of total capacity obtained from 3.8 to 4.25 V. The electrochemical performance will be discussed in detail in Section 3.4. For the materials synthesized using the eutectic ratio of LiCl−KCl, it is apparent that the 4.0 V plateau increased with increasing synthesis temperature from 650 to 850 °C. Higher synthesis temperatures may induce more oxygen vacancies, which can be compensated for by the reduction of Mn.[31,32] The formation of more rock-salt $Li_xNi_{1-x}O$-type impurities may also occur during high-temperature synthesis, along with the formation of Ni−Mn oxides in Li-deficient environments.[33] The presence of these impurities can increase the Mn/Ni ratio in the disordered spinel phase, increasing the Mn^{3+} content without the formation of oxygen vacancies.[10] A comparison of the lattice parameter, *a*, with the approximate Mn^{3+} content for the full series of materials shows that both properties increased as the synthesis temperature increased from 650 to 850 °C for each flux composition (Figure 2d). This is rationalized by the larger ionic radius of Mn^{3+} (0.65 Å) compared to that of Mn^{4+} (0.54 Å);[34] the increased lattice parameter in the samples suggests an expansion due to higher Mn^{3+} content.[15] For example, material synthesized at 650 °C using the eutectic salt composition had a lattice constant of 8.1581(5) Å and an average Mn^{3+} content of 5.87%. Increasing the synthesis temperature to 850 °C using the same salt medium resulted in a lattice constant of 8.2167(3) Å and a Mn^{3+} content of 50.32% for the sample. The trend for sample properties was not as clear when varying the molten salt composition at a single temperature. At lower proportions of LiCl, there was a more significant increase in the lattice constant and Mn^{3+} content which may be due to poorer LNMO crystal formation in this molten salt composition. The high melting temperature of 688 °C for the 20:80 LiCl/KCl flux as well as decreased Li^+ mobility as the K^+ concentration was increased may have impacted the formation of the spinel phase.[35]

Raman spectroscopy was also used to evaluate each sample because it is sensitive to the local crystal structure. It is useful to determine the degree of cation ordering in LNMO because XRD cannot detect small amounts of ordered phases due to the technique's poor chemical contrast for distinguishing Ni and Mn.[36] Figure 2e−g shows the Raman spectra for the materials synthesized at 650, 750, and 850 °C, respectively. Peaks at 650 cm^{-1} represent the symmetric Mn−O stretching vibration in a MnO_6 octahedra, while peaks at 490 and 390 cm^{-1} are assigned to the Ni^{2+}−O stretching mode.[11,22] Due to

https://dx.doi.org/10.1021/acs.inorgchem.0c01042
Inorg. Chem. XXXX, XXX, XXX−XXX

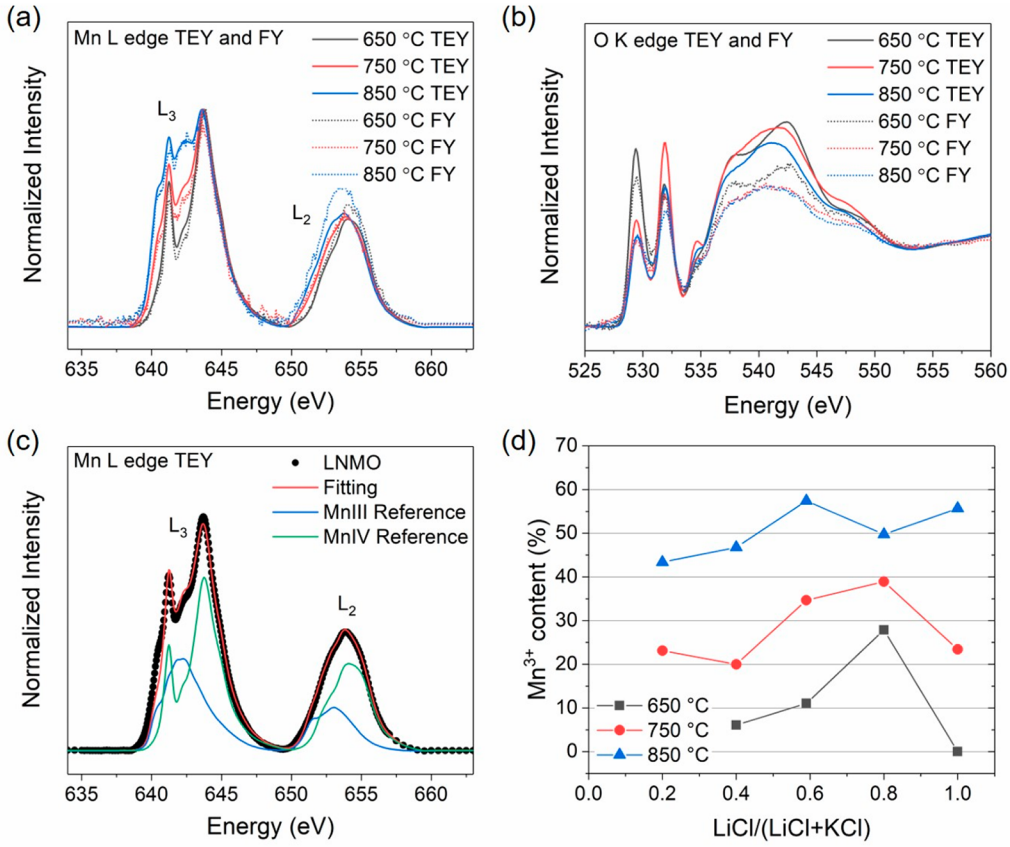

Figure 4. Comparison of TEY and FY collection modes for (a) Mn L-edge spectra and (b) O K-edge spectra of LNMO prepared using eutectic LiCl−KCl at 650, 750, and 850 °C. (c) Example of linear combination spectra for the LNMO sample prepared using 59:41 LiCl−KCl at 750 °C. Mn(III) reference: Mn_2O_3. Mn(IV) reference: LNMO prepared using 100:0 LiCl−KCl at 650 °C. (d) Approximate Mn^{3+} content calculated from Mn L-edge XAS fittings.

the separated Ni and Mn sites, peak splitting at about 630 cm^{-1} is expected for the lower-symmetry, ordered $P4_332$ structure along with the appearance of additional peaks at 239, 218, and 160 cm^{-1}. Broad peaks without splitting show the predominance of the disordered spinel phase for all samples, which is consistent with XRD data (Figure S1). The features of the Ni^{2+}−O stretching become less intense as the temperature increases, most noticeably for samples prepared with 20:80 LiCl−KCl at 750 and 850 °C and with 100:0 LiCl−KCl at 850 °C, indicating a greater degree of cation disorder. The sample prepared with 100:0 LiCl−KCl at 850 °C also has a noticeable peak shift likely due to the increased impurity phases. From the structural characterizations, all materials synthesized belong to the $Fd\bar{3}m$ space group. The extent of disorder increased with increasing temperature for each molten salt composition investigated and is coupled with the Mn^{3+} content.

Synchrotron XAS was also used to further characterize the electronic structure of the materials at different length scales. Soft XAS is a technique capable of probing transition metal (TM) oxidation states and local environments in a compound with element specificity and surface sensitivity.[37] The total electron yield (TEY) detection mode probes 2−5 nm of the material's surface, while fluorescence yield (FY) mode collects signal at up to 50 nm, which is still considered subsurface for large particles in the present case. Soft XAS probes the unoccupied states through TM 2p−3d transitions at the TM L-edge and O 1s−2p transitions at the O K-edge.[30,38] The TM L-edge is divided due to spin−orbit splitting, with the L_3 edge at lower energy and the L_2 edge at higher energy.

Figure 3a−c shows the Mn L-edges collected in TEY mode for LNMO synthesized in different LiCl−KCl compositions at various temperatures. For Mn, the intensity ratio of the high-energy and low-energy L_3 shoulders is indicative of the oxidation state, with a higher ratio indicating more oxidation. A decrease in the high-to-low L_3 shoulder intensity ratio and an increase in the total peak areas were seen as the synthesis temperature increased, indicating Mn reduction or, in other words, an increased Mn^{3+} contribution. Varying the salt ratio at a fixed temperature resulted in a slight change in the Mn oxidation state for each temperature series, but no discernible trend appeared as the ratio was varied across the phase diagram. At 650 °C (Figure 3a) and 750 °C (Figure 3b), 80:20 LiCl−KCl produced the samples with the most reduced Mn. At 850 °C (Figure 3c), ratios of 59:41 and 100:0 LiCl−KCl led to samples with the most Mn reduction.

The Ni L-edges (Figure 3d−f) showed no change for any of the samples, indicating that all pristine materials have Ni in the expected 2+ oxidation state despite the synthesis method. The O K-edge pre-edge region with sharp peaks from 527 to 534 eV originates from O 2p and TM 3d hybridization. Increasing pre-edge peak areas correspond to increasing hybridization and should also correlate with increasing TM oxidation states.[30] For LNMO samples, total pre-edge peak areas of the O K-edge spectra (Figure 3g−i) are generally smaller for samples that

https://dx.doi.org/10.1021/acs.inorgchem.0c01042
Inorg. Chem. XXXX, XXX, XXX−XXX

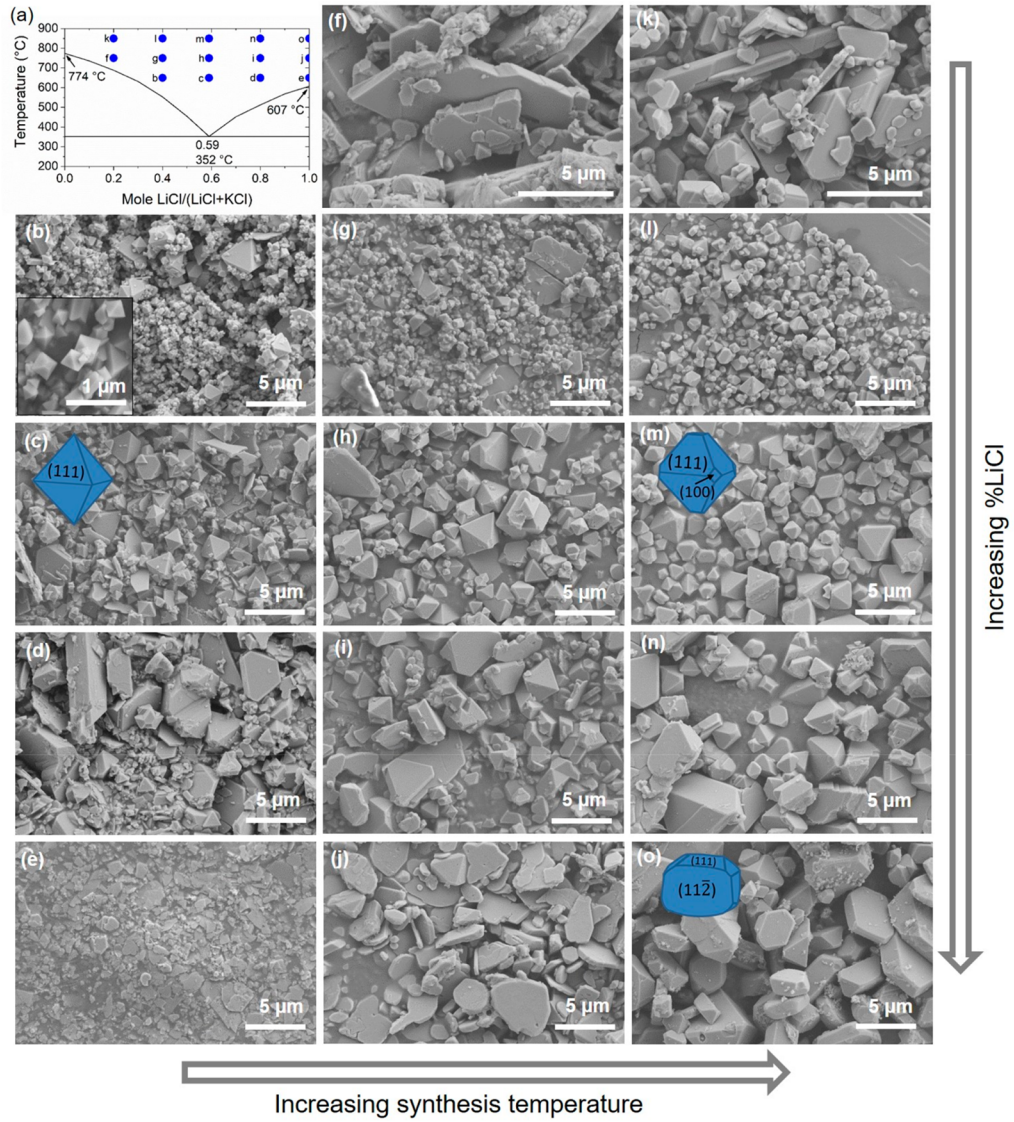

Figure 5. (a) LiCl–KCl phase diagram. SEM images of LNMO prepared at (b–e) 650 °C, (f–j) 750 °C, and (k–o) 850 °C with LiCl–KCl compositions of (f, k) 20:80 (irregular particles), (b, g, l) 40:60 (octahedrons), (c, h, m) 59:41 (octahedrons), (d, i, n) 80:20 (octahedrons and plates), and (e, j, o) 100:0 (plates).

also contain Mn at lower oxidation states, confirming the agreement of TM and oxygen soft XAS data.

To compare the difference in the surface and subsurface electronic states, Mn L-edge and O K-edge spectra in both the TEY and FY modes for LNMO materials synthesized using the eutectic ratio of LiCl and KCl at each temperature are shown in Figure 4a,b. The near overlap between the TEY and FY spectra indicates similarity between surface and subsurface Mn oxidation states for all materials; however, the slightly higher intensity for the TEY mode at lower photon energy suggests that the particle surfaces are slightly more reduced than the subsurface. For the O K-edge, a similar trend of decreasing pre-edge total area is seen as temperature increases for both detection modes. The intensity ratio of the lower-energy to higher-energy O K-edge pre-edge peaks also provides useful information on TM–O hybridization with lower ratios corresponding to samples with increased Mn^{3+}.[39] The intensity ratio decreases from 650 to 750 °C but increases slightly from 750 to 850 °C; however, general trends in soft XAS data are in agreement when the temperature is varied and the salt ratio is fixed as well as vice versa. Supporting Information Figure S2 shows the FY spectra for the full sample set.

We performed a linear combination using a Mn_2O_3 sample as a Mn^{3+} reference and the LNMO sample containing the lowest L_3 peak area as a Mn^{4+} reference (assuming no Mn^{3+}) in the TEY collection mode in order to calculate the approximate relative percentages of Mn^{3+} in each sample. Figure 4c displays an example spectrum of the linear combination peak fitting for the LNMO sample prepared using a eutectic LiCl–KCl flux at 750 °C. We compared this approximation to the Mn^{3+} content determined from electrochemical data (previously compared to lattice parameter in Figure 2d). These results showed general agreement of the Mn^{3+} content calculated by both methods (compare Figures 2d and 4d). Discrepancies may originate from impurity content as spectroscopic methods provide only global, average oxidation state information and do not differentiate between multiple crystal structures that may be present. These impurities may be electrochemically inactive and contain mixed Mn^{3+} and Mn^{4+} states. Once again, we observed that the Mn^{3+} content increased with higher synthesis

https://dx.doi.org/10.1021/acs.inorgchem.0c01042
Inorg. Chem. XXXX, XXX, XXX–XXX

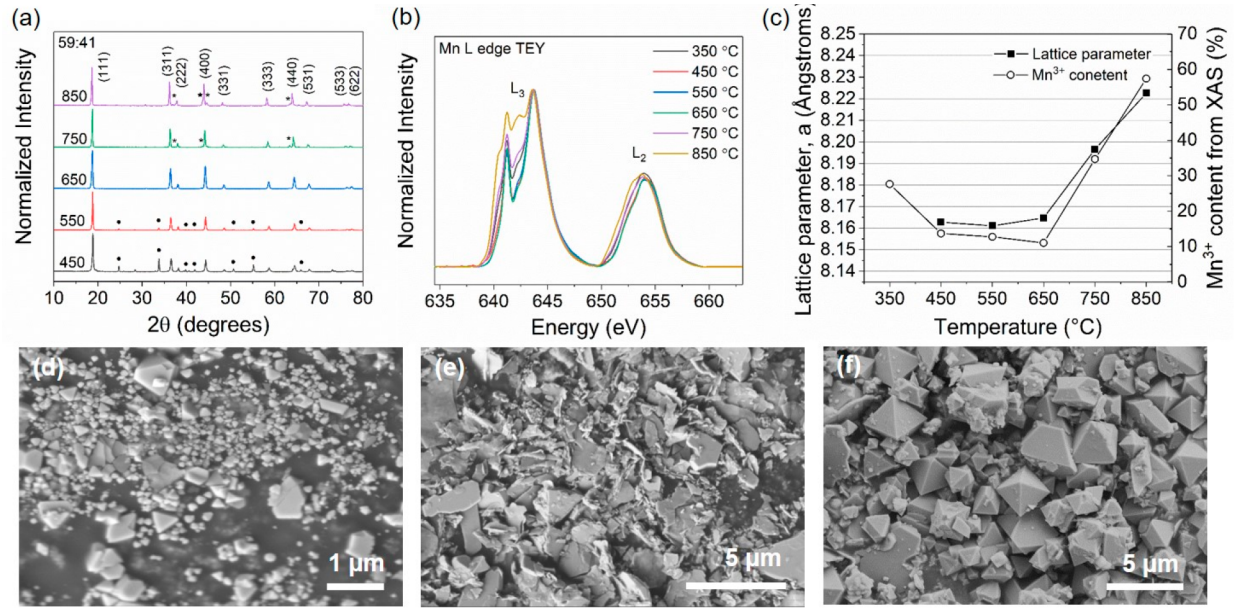

Figure 6. (a) XRD patterns of LNMO prepared using eutectic LiCl−KCl at various temperatures. $Fd\bar{3}m$ Miller indices are labeled. Asterisks indicate the location of rock-salt impurities. Dots indicate the location of the Mn_2O_3 intermediate phase. (b) Mn L-edge XAS spectra of LNMO prepared using eutectic LiCl−KCl at various temperatures. (c) Comparison of the lattice parameter and approximate Mn^{3+} content. SEM images of LNMO synthesized in 59:41 LiCl−KCl at (d) 350, (e) 450, and (f) 550 °C.

temperatures, although no clear trend was seen as LiCl−KCl compositions were varied. The electrochemical data represents a bulk analysis while soft XAS is a highly surface-sensitive technique. Therefore, on the basis of our characterizations we believe the surface and bulk electronic properties of individual samples to be generally comparable and representative.

In summary, (1) all LNMO samples were indexed by XRD to the $Fd\bar{3}m$ space group with increasing rock-salt impurities as temperatures increased. (2) Lattice constants and Mn^{3+} content both increased at higher synthesis temperatures due to the larger ionic radius of Mn^{3+} compared to that of stoichiometric Mn^{4+}. (3) Raman spectroscopy also confirmed the $Fd\bar{3}m$ assignments, with increasing cation disorder as synthesis temperature increased. (4) Soft XAS showed that Mn was more reduced and TM−O hybridization decreased for samples prepared at higher temperatures. (5) The Mn^{3+} content approximated from both soft XAS data and electrochemical characterization was in agreement, supporting the theory that higher synthesis temperatures lead to a reduction of Mn, which may be induced though the presence of oxygen vacancies, excess metal cations, or impurity phases. However, (6) none of the structural characterization methods showed clear trends for samples prepared at fixed temperatures, indicating that the Mn^{3+} content is not strongly dependent on the LiCl−KCl molten salt composition.

3.2. Influence of Molten Salt Composition and Synthesis Temperature on the Morphology and Particle Size. In order to determine the influence of the molten salt composition and synthesis temperature on the LNMO particle morphology and size, samples were analyzed by SEM. Each composition and temperature combination investigated is plotted on the phase diagram of LiCl and KCl in Figure 5a. Morphological changes were most clearly seen as the salt composition was varied. It has been observed with perovskite $LaMnO_3$ prepared in both eutectic LiCl−KCl and NaCl−KCl that the synthesis temperature did not change the particle morphology or size, while the change in flux had a significant effect on both.[40] This is consistent with our observations. At a fixed salt flux composition, samples appeared to have a dominant morphology independent of the synthesis temperature.

The growth rates of the crystal surface differ due to differences in surface energies. The equilibrium shape of crystals is often predicted to be composed of the lowest-energy facets; however, crystals may not reach their equilibrium morphology during growth because kinetic factors dictate the final shape.[41] Reaction conditions influence the nucleation and growth rates, where the ratio of these determines the particle size and morphology. In molten salt methods, nucleation and growth are determined by both the melting temperature of the flux and the composite properties of the flux, including melting temperature, viscosity, ionic radii, and precursor solubility.[42] In fluxes with lower melting temperatures, there is a lower ratio between the nucleation and growth rate, and as a result, larger crystals with wider size distributions are obtained.[42] Higher surface energy facets that are kinetically favorable may be stabilized in different flux environments, although the influence of the chemical properties of the flux on particle morphology has not been fully revealed.

The low melting temperature of 353 °C for the eutectic ratio of 59:41 LiCl/KCl salt facilitated the diffusion of the raw materials, allowing crystal formation and the thermodynamically favorable morphology of octahedrons enclosed by (111) facets to predominate at a low synthesis temperature of 650 °C (Figure 5c).[25] The 40:60 mixture, in which the molar ratio of both salts is similarly balanced, may have composite properties similar to the eutectic ratio and also led to the formation of octahedrons (Figure 5b). This salt ratio has a higher melting temperature of 553 °C, only 97 °C below the 650 °C synthesis temperature, so the nucleation to growth ratio is predicted to be higher. This led to the formation of smaller octahedron particles overall (~0.5 μm) compared to the eutectic

https://dx.doi.org/10.1021/acs.inorgchem.0c01042
Inorg. Chem. XXXX, XXX, XXX−XXX

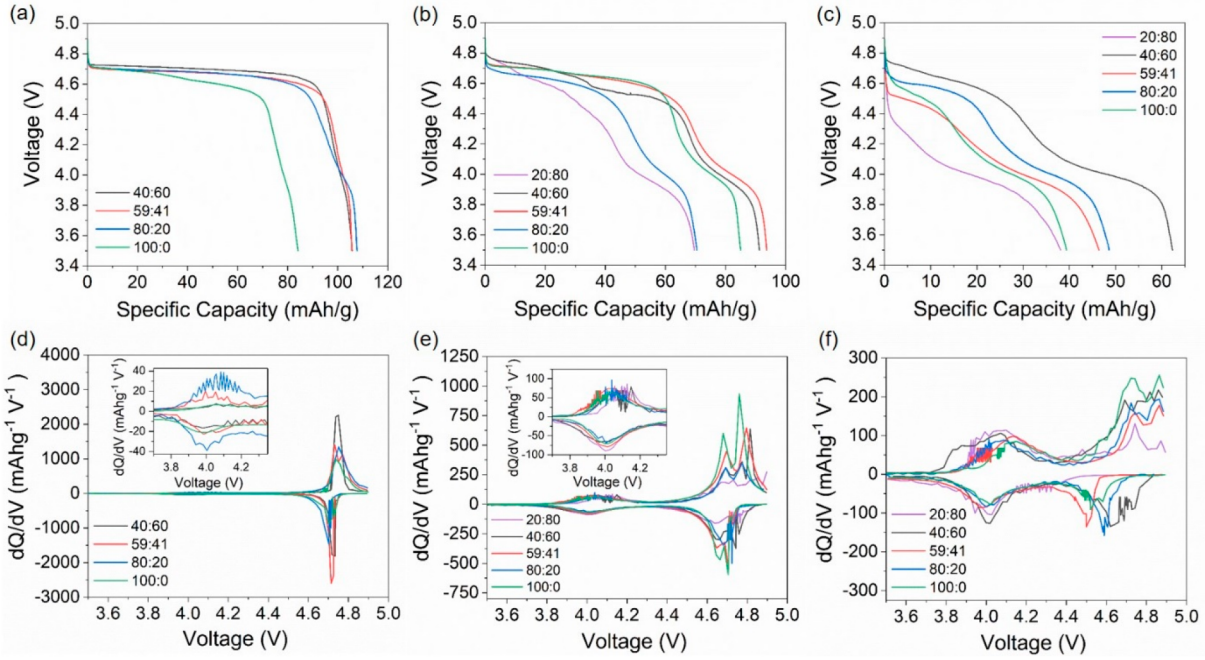

Figure 7. First discharge profiles of LNMO prepared with different LiCl–KCl compositions at (a) 650, (b) 750, and (c) 850 °C between 3.5 and 4.9 V at 0.1 C. The second discharge is shown for the sample prepared with 20:80 LiCl–KCl at 750 °C. dQ/dV plots for samples prepared at (d) 650, (e) 750, and (f) 850 °C. Insets show the region between 3.7 and 4.35 V. The ratios in the figure represent the molar ratio LiCl–KCl. The measurements were performed at 22 °C.

composition (~1.0 μm) at 650 °C. For the lower melting temperature eutectic LiCl–KCl media, particle formation was predominantly in the liquid phase and larger particles were able to form rapidly. Particles with similar morphologies also form at 750 °C (Figure 5g,h) and 850 °C (Figure 5l,m) in these fluxes for the same reasons.

The flux ratios with a higher proportion of LiCl to KCl (80% LiCl in Figure 5d,i,n and 100% LiCl in Figure 5e,j,o) created favorable conditions to stabilize higher-energy facets, giving rise to more kinetically driven plate-like morphologies with $(11\bar{2})$ surfaces in addition to thermodynamically stable octahedrons.[28] This is due to both the higher melting points and changes in chemical properties of the flux. Similarly, with a 20% LiCl composition at 750 and 850 °C syntheses (Figure 5f,k), irregular and plate-like morphologies predominated.

At a fixed salt flux composition, increasing temperatures did not affect particle size significantly. Supporting Information Figure S3 shows the size distribution histograms for each material based on the SEM images and averaging the diameter of 100 randomly selected particles. Increasing temperature in the investigated range did not change the overall particle morphology but allowed for continued growth of already predominating facets. For example, the eutectic ratio led to the formation of octahedrons enclosed by (111) facets of approximately 1.0 μm diameter at all temperatures 650 to 850 °C with increasing (100) truncation visible as the temperature increased (Figure 5c,h,m). Likewise, 100% LiCl allowed kinetically stable $(11\bar{2})$ facets to predominate, resulting in plate-like particles at all temperatures (Figure 5e,j,o) with the development of more (111) facets as temperatures increased, leading to thicker plates.[43,44] Increasing amounts of salt flux could be used to narrow the particle size distribution. However, large amounts of salt flux are disadvantageous as it may become more difficult to separate synthesized materials from the salt residue.[25,45]

In summary, our SEM analysis suggests that the morphology and size of LNMO synthesized by the molten salt method is more dependent on the LiCl–KCl composition than the synthesis temperature. Well-defined octahedrons, plates, and irregularly shaped particles were all synthesized through a variation of the salt composition. The size distribution was also found to broaden slightly with increasing temperatures.

3.3. Investigating Particle Formation Using a Eutectic LiCl–KCl Molten Salt Ratio (59:41) at Different Synthesis Temperatures. To further investigate the low-melting-temperature eutectic LiCl–KCl composition with respect to the formation of LNMO particles, material was synthesized using the eutectic flux at low synthesis temperatures of 350, 450, and 550 °C. Figure 6a compares the XRD patterns for these materials to those previously discussed, which were synthesized at 650, 750, and 850 °C. It should be noted that the synthesis at 350 °C is close to the 352 °C melting temperature for the flux, so a molten reaction may not have been complete, resulting in a very small yield of powder sample (<50 mg, which is ~5.0% yield for a normal batch), which was not studied by XRD analysis. From the 450 °C synthesis sample, the pattern indicative of the $Fd\bar{3}m$ space group is present, suggesting that LNMO formation begins below this temperature. However, the 450 °C sample pattern also showed significant peaks of a Mn_2O_3 intermediate phase (indicated by dots) which occurred during the open air calcination.[46] At 550 °C, the intermediate phase decreases as the spinel phase continues to form. By 650 °C, a pure-phase spinel is obtained. Samples synthesized at 750 and 850 °C also show the spinel phase with increasing contributions from $Li_xNi_{1-x}O$-type impurity phases.

TEY-mode Mn L-edge soft XAS spectra for low-temperature synthesized samples are shown in Figure 6b. Approximate Mn^{3+} content was determined from the XAS data, as previously discussed. Supporting Information Figure S4 contains the Mn

https://dx.doi.org/10.1021/acs.inorgchem.0c01042
Inorg. Chem. XXXX, XXX, XXX–XXX

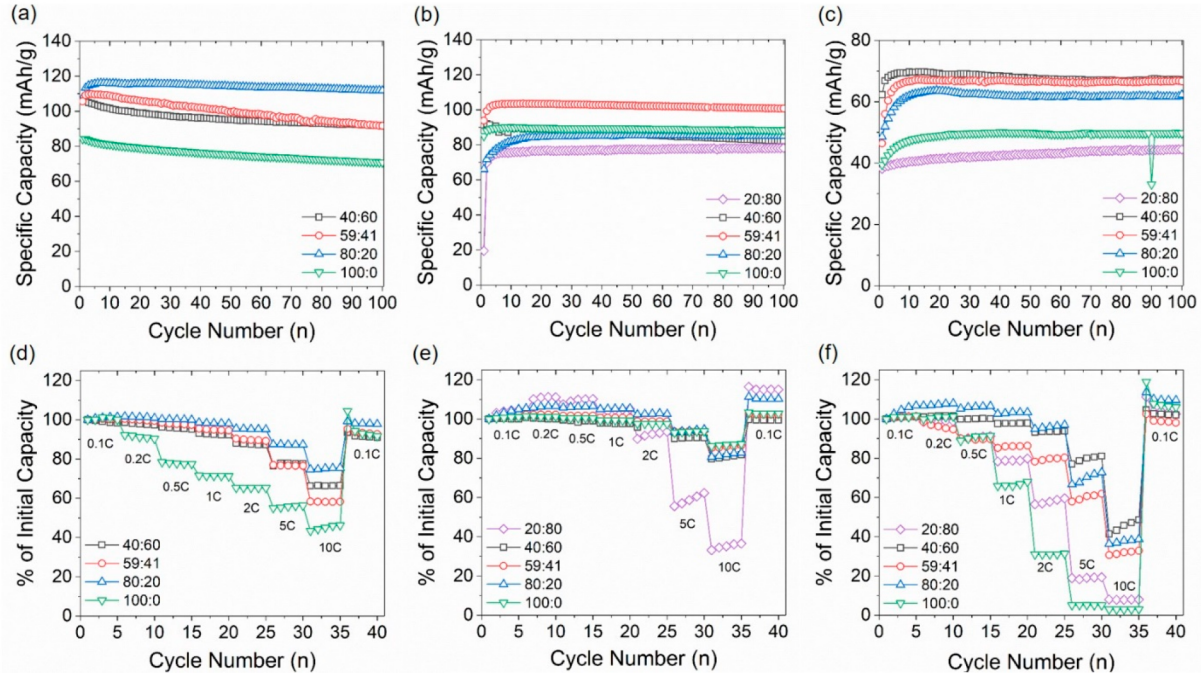

Figure 8. Cycling performance of LNMO prepared with different LiCl−KCl compositions at (a) 650, (b) 750, and (c) 850 °C between 3.5 and 4.9 V at 0.1 C. Rate capability with constant charging at 0.1 C and discharging at various C rates for samples prepared at (d) 650, (e) 750, and (f) 850 °C. The ratios in the figure represent the molar ratio LiCl−KCl. The measurements were performed at 22 °C.

L-edge FY and Ni L-edge and O K-edge TEY and FY spectra. Changes in the lattice parameter, *a*, and the Mn^{3+} content are plotted as a function of increasing synthesis temperature in Figure 6c. The trend of increasing lattice parameter with higher temperature holds only for temperatures above 650 °C. From 450 to 650 °C, the lattice parameter is constant at ∼8.16 Å. This is consistent with the literature as cation disordering and the introduction of Mn^{3+} are expected to occur with syntheses above 700 °C.[11] With increasing temperature, more oxygen vacancies and impurities and, in turn, Mn^{3+} are introduced. The sample synthesized at 350 °C had a larger Mn^{3+} content than those in the 450 to 650 °C range, which is likely due to the unreacted precursors containing Mn in lower oxidation states or the significant presence of Mn_2O_3, as shown by the XRD pattern (Figure 6a).

The SEM images for LNMO synthesized at low temperatures are shown in Figure 6d−f. Due to the low-temperature formation of the liquid reaction media in the eutectic salt flux, the development of nanometer-sized LNMO octahedrons appears to begin as low as 350 °C (Figure 6d). Micrometer-sized, irregularly shaped particles were also visible and may be unreacted precursors or intermediate-phase particles. At 450 °C (Figure 6e), thin, sheet-like crystals appeared along with the nanometer LNMO octahedrons, indicating that precursors or intermediates had still not completely reacted. By 550 °C (Figure 6f), well-developed, micrometer-sized octahedrons predominated, with a morphology and size comparable to those of materials synthesized at 650 °C (Figure 5c).

In summary, using a low-melting-temperature eutectic salt mixture of LiCl and KCl allows LNMO crystal formation to begin as low as 350 °C, as soon as the molten flux is formed with pure-phase, micrometer-sized crystals fully developed by 550 °C. Increased cation disorder and Mn^{3+} content appear at synthesis temperatures above 700 °C.

3.4. Influence of Molten Salt Composition and Synthesis Temperature on Electrochemical Performance. In order to evaluate the electrochemical performance of LNMO synthesized under different molten salt synthesis conditions, coin cells were prepared and cycled at 22 °C from 3.5 to 4.9 V under galvanostatic conditions at 0.1 C (1 C = 148 mAh/g). The first discharge profile for each material synthesized with different molten salt compositions at 650, 750, and 850 °C, is shown in Figure 7a−c, respectively. For the 650 °C synthesis series (Figure 7a), fluxes with 40, 59, and 80% LiCl produced materials with discharge capacities of 105.8, 105.6, and 107.7 mAh/g. Material synthesized with 100% LiCl gave a 84.15 mAh/g initial discharge capacity. This decrease in capacity compared to the rest of the series is likely due to the significantly different morphology produced by using 100% LiCl salt flux. For the 750 °C synthesis series (Figure 7b), the eutectic ratio produced the material with the highest capacity at 93.72 mAh/g, while the 40:60 LiCl−KCl mixture produced the best-performing material for the 850 °C series (Figure 7c) with a 62.3 mAh/g discharge capacity. The initial capacity obtained from samples drastically decreased with increasing synthesis temperatures. This corresponds to a significant increase in the 4.0 V plateau with increased temperature. The decrease in capacity may therefore be attributed to the increase in structural disorder and impurity phases accompanying the Mn reduction as synthesis temperatures increase.

To further illustrate this observation, d*Q*/d*V* plots are shown in Figure 7d−f. The change in Mn^{3+} content represented by the peak at 4.0 V is much more significant between the samples synthesized at various temperatures, rather than by those synthesized at a single temperature using various salt compositions. The huge variation in Mn^{3+}, determined from the percent of capacity obtained from 3.8 to 4.25 V, increases from approximately 5 to 10% for materials synthesized at 650

https://dx.doi.org/10.1021/acs.inorgchem.0c01042
Inorg. Chem. XXXX, XXX, XXX−XXX

°C, from 22 to 33% for those synthesized at 750 °C, and from 44 to 68% at 850 °C synthesis. The majority of the capacity for the 650 °C synthesis series is obtained from the major voltage plateaus at ∼4.7 V, which corresponds to the Ni^{2+}/Ni^{4+} redox process and leads to higher capacities. For the 750 and 850 °C series, the reduced contribution to the capacity from Ni redox may result from increased concentrations of electrochemically inactive Ni rock-salt impurities or an unfavorably high degree of cation disorder.

The location of peaks in the dQ/dV plots is also informative. The separation of the peaks at 4.7 V is indicative of the extent of order/disorder, where separation by >50 mV is considered disordered and separation of <30 mV is considered ordered for spinel LNMO.[16] The quality of the dQ/dV plots is not high enough to confidently discern the location of these peaks, but for the 750 and 850 °C synthesis samples, increasing separation into two peaks at ∼4.7 V is clear qualitatively, indicating a higher extent of cation disorder, which is consistent with previous structural characterizations discussed in this work.

Long-term cycling data is shown is Figure 8a−c. Coin cells were cycled 100 times at a rate of 0.1 C. There is an initial increase in the capacity for nearly all samples due to electrochemical activation.[47] After 100 cycles, all samples show high capacity retentions of >89%. The 850 °C series show the highest capacity retentions at 97.0−99.9% as a result of its much lower capacity, which reduces side reactions with the electrolyte and allows for longer reversible cycling without capacity fading. A single trend in the discharge capacity as molten salt compositions are varied is not seen for a series of samples prepared at fixed temperatures. At a fixed temperature, a smaller variation in Mn^{3+} is seen compared to samples prepared at different temperatures, and increasing Mn^{3+} does not necessarily correspond to increasing capacity. The Mn^{3+} content, therefore, does not fully explain the differences in performance for material synthesized at fixed temperatures, but their performance differences originate from changes in morphology, size, extent of disorder, or a synergistic combination of these characteristics. Supporting Information Figure S5 shows both the charge and discharge capacities over 100 cycles as well as the Coulombic efficiencies.

Rate capability tests were performed for all materials with 0.1 C charging and 0.1, 0.2, 0.5, 1, 2, 5, and 10 C discharge rates. Plots were normalized to the first discharge capacity after three activation cycles at 0.1 C. In the 650 °C series (Figure 8d), 80% LiCl flux gave rise to the material with the best rate performance at all C rates due to the slight increase in Mn^{3+} improving the electronic conductivity compared to that of other samples in the series (Figures 4d and 7a).[48,49] For the sample synthesized with 100% LiCl, less Mn^{3+} (Figures 4d and 7a) and the presence of $(11\bar{2})$ facets (Figure 5e) led to inferior rate performance. Octahedrons enclosed by (111) facets are expected to have better rate capability than the $(11\bar{2})$ facet-containing plates due to better Li^+ diffusion kinetics.[28,50]

For samples synthesized at 750 °C (Figure 8e), increased Mn^{3+} content led to the highest rate capability for all samples, maintaining up to 87% of the initial capacity at 10 C for the best performing sample. The sample synthesized with 20% LiCl gave the poorest rate performance of the series, which may be attributed to its irregular morphology and large particle size (>2 μm), increasing the lithium diffusion path.[21] For the set of samples synthesized at 850 °C (Figure 8f), the presence of truncating (100) facets (Figures 5l−n) was expected to show improved Li^+ diffusion compared to 100% (111) facets;[22] however, the significant percentage of Mn^{3+} appeared to have a detrimental effect on the rate capability. This is likely due to increased impurity phases which may also be responsible for the reduced Mn. Meanwhile, the slightly smaller octahedrons synthesized with 40% LiCl (Figure 5l) give the best performance at each C rate; nanosized particles have improved rate performance due to smaller Li^+ diffusion pathways.[31] Irregularly shaped samples synthesized in 20% LiCl at 750 and 850 °C and plate-like samples synthesized with 100% LiCl at 850 °C representing either end of the LiCl composition spectrum gave the poorest rate performances. The increased impurity phases, large size, and larger extent of cation disorder explain the overall low capacity and the significant loss of capacity at faster C rates.[51]

In LNMO, Mn^{3+} is expected to be redox-active and can lead to better electrochemical performance and rate capability than the perfectly stoichiometric material. More Mn^{3+} was expected to improve the rate capability due to the increased lattice parameter, improving Li^+ diffusion;[52] however, the accompanying rock-salt $Li_xNi_{1-x}O$-type impurities that also occur with increased synthesis temperatures and an increase in cation disorder may have been detrimental to performance. In summary, our electrochemical data suggests that there is an optimum concentration of Mn^{3+} between ∼10 and 25% that can improve the electrochemical performance. Concentrations in this range provide increased ionic conductivities in the disordered spinel, while concentrations larger than this are likely due to a large presence of reduced Mn in segregated impurity phases. Controlled postsynthesis annealing and slow cooling to maintain Mn^{3+} but reduce impurity formation would give further insights into the isolated effects of Mn^{3+} content on LNMO performance. It is also important to consider that larger concentrations of Mn^{3+} at the materials surface may lead to increased transition-metal dissolution during high voltage operation. Further optimization of Mn^{3+} in LNMO must take dissolution behavior into account.[7]

4. CONCLUSIONS

LNMO was synthesized via a molten salt method using LiCl and KCl. Synthesis parameters including molten salt composition and the maximum synthesis temperature were carefully and systematically tuned to determine their effects on material properties and electrochemical performance. Varying the composition of LiCl and KCl across the phase diagram, we have tuned the melting temperature of the flux medium to investigate the impact on particle formation and growth. A series of materials differing in morphology and particle size as well as Mn oxidation states were acquired. We have identified a series of materials with similar sizes and morphologies but with significantly different Mn^{3+} content ranging from ∼7 to ∼25 to ∼50% that are dependent on the synthesis temperatures of 650, 750, or 850 °C, respectively. Similarly, materials with similar Mn^{3+} contents, differing in size and overall morphology, are dependent on the composition of the molten salt. The change in particle morphology can therefore be attributed to the properties of the salt flux more so than the difference in the synthesis temperature above the melting temperature. A low-melting-temperature eutectic ratio of LiCl−KCl gave rise to thermodynamically favorable octahedrons enclosed by (111) facets forming at as low as the composite melting temperature of 350 °C and developing into micrometer-sized particles by 550 °C.

https://dx.doi.org/10.1021/acs.inorgchem.0c01042
Inorg. Chem. XXXX, XXX, XXX−XXX

Electrochemical characterizations showed that despite increased Mn^{3+} content induced through high-temperature syntheses, the accompanying high concentrations of rock-salt impurities and severe cation disorder can be detrimental to the capacity and rate performance of spinel LNMO. The sample synthesized using a salt flux of 80:20 LiCl−KCl at 650 °C showed the best performance overall with a maximum discharge capacity of 115.8 mAh/g and a capacity retention of 96.8% after 100 cycles. Its rate capability was comparable to those in the 750 °C series, with a capacity of 84 mAh/g (75% of the capacity at 0.1 C) at 10 C. Between ∼10 and 25% Mn^{3+} content may be an ideal quantity to give high capacity and improved rate capability. Over ∼30% bulk Mn^{3+} content began to hinder the performance of LNMO as segregated impurity phases likely contributed to the large amounts of reduced Mn detected.

We have investigated several independent and coupled material characteristics of LNMO including the crystal structure, electronic structure, and morphology as molten salt synthesis parameters were systematically tuned. Molten salt synthesis methods can therefore be used to rationally design LNMO with specific facets and with controllable amounts of Mn^{3+}. Materials can be further modified through postprocessing techniques such as annealing to improve the electrochemical performance and minimize impurity phases. Further studies in the synthesis of LNMO are needed to continue to decouple the influence of Mn^{3+} content and its associated parameters.

■ ASSOCIATED CONTENT

Supporting Information

The Supporting Information is available free of charge at https://pubs.acs.org/doi/10.1021/acs.inorgchem.0c01042.

XRD patterns of LNMO prepared with various LiCl−KCl compositions at different temperatures; structural information obtained from the Rietveld refinement analysis; soft XAS spectra of LNMO prepared with various LiCl−KCl compositions at different temperatures in the FY collection mode; size distribution histograms based on SEM images of LNMO prepared with various LiCl−KCl compositions at different temperatures; soft XAS spectra of LNMO prepared using eutectic LiCl−KCl at various temperatures; charge and discharge capacities and Coulombic efficiency of LNMO prepared with various LiCl−KCl compositions at different temperatures (PDF)

■ AUTHOR INFORMATION

Corresponding Author

Feng Lin − *Department of Chemistry, Virginia Tech, Blacksburg, Virginia 24061, United States;* orcid.org/0000-0002-3729-3148; Email: fenglin@vt.edu

Authors

Stephanie L. Spence − *Department of Chemistry, Virginia Tech, Blacksburg, Virginia 24061, United States;* orcid.org/0000-0002-7039-3554

Zhengrui Xu − *Department of Chemistry, Virginia Tech, Blacksburg, Virginia 24061, United States*

Sami Sainio − *Stanford Synchrotron Radiation Lightsource, SLAC National Accelerator Laboratory, Menlo Park, California 94035, United States*

Dennis Nordlund − *Stanford Synchrotron Radiation Lightsource, SLAC National Accelerator Laboratory, Menlo Park, California 94035, United States*

Complete contact information is available at: https://pubs.acs.org/10.1021/acs.inorgchem.0c01042

Notes

The authors declare no competing financial interest.

■ ACKNOWLEDGMENTS

We acknowledge the Donors of the American Chemical Society Petroleum Research Fund for partial support of this research on the materials synthesis portion. The battery portion of the work was supported by the National Science Foundation under contract DMR 1832613 and the Institute for Critical Technology and Applied Science at Virginia Tech. Use of the Stanford Synchrotron Radiation Lightsource, SLAC National Accelerator Laboratory, is supported by the U.S. Department of Energy, Office of Science, Office of Basic Energy Sciences under contract no. DE-AC02-76SF00515. S.S. acknowledges Muhammad Mominur Rahman for SEM image acquisition.

■ REFERENCES

(1) Tarascon, J. M.; Armand, M. Issues and Challenges Facing Rechargeable Lithium Batteries. *Nature* **2001**, *414* (6861), 359−367.

(2) Armand, M.; Tarascon, J. M. Building Better Batteries. *Nature* **2008**, *451* (7179), 652−657.

(3) Patoux, S.; Daniel, L.; Bourbon, C.; Lignier, H.; Pagano, C.; Le Cras, F.; Jouanneau, S.; Martinet, S. High Voltage Spinel Oxides for Li-Ion Batteries: From the Material Research to the Application. *J. Power Sources* **2009**, *189* (1), 344−352.

(4) Santhanam, R.; Rambabu, B. Research Progress in High Voltage Spinel $LiNi_{0.5}Mn_{1.5}O_4$ Material. *J. Power Sources* **2010**, *195* (17), 5442−5451.

(5) Zhong, Q. Synthesis and Electrochemistry of $LiNi_xMn_{2-x}O_4$. *J. Electrochem. Soc.* **1997**, *144* (1), 205.

(6) Ma, J.; Hu, P.; Cui, G.; Chen, L. Surface and Interface Issues in Spinel $LiNi_{0.5}Mn_{1.5}O_4$: Insights into a Potential Cathode Material for High Energy Density Lithium Ion Batteries. *Chem. Mater.* **2016**, *28* (11), 3578−3606.

(7) Manthiram, A.; Chemelewski, K.; Lee, E. S. A Perspective on the High-Voltage $LiMn_{1.5}Ni_{0.5}O_4$ spinel Cathode for Lithium-Ion Batteries. *Energy Environ. Sci.* **2014**, *7*, 1339−1350.

(8) Kim, J. H.; Myung, S. T.; Yoon, C. S.; Kang, S. G.; Sun, Y. K. Comparative Study of $LiNi_{0.5}Mn_{1.5}O_{4-\delta}$ and $LiNi_{0.5}Mn_{1.5}O_4$ Cathodes Having Two Crystallographic Structures: Fd3m and $P4_332$. *Chem. Mater.* **2004**, *16* (5), 906−914.

(9) Julien, C. M.; Mauger, A. Review of 5-V Electrodes for Li-Ion Batteries: Status and Trends. *Ionics* **2013**, *19* (7), 951−988.

(10) Aktekin, B.; Valvo, M.; Smith, R. I.; Sørby, M. H.; Lodi Marzano, F.; Zipprich, W.; Brandell, D.; Edström, K.; Brant, W. R. Cation Ordering and Oxygen Release in $LiNi_{0.5-X}Mn_{1.5+X}O_{4-y}$ (LNMO): In Situ Neutron Diffraction and Performance in Li Ion Full Cells. *ACS Appl. Energy Mater.* **2019**, *2* (5), 3323−3335.

(11) Song, J.; Shin, D. W.; Lu, Y.; Amos, C. D.; Manthiram, A.; Goodenough, J. B. Role of Oxygen Vacancies on the Performance of $Li[Ni_{0.5-X}Mn_{1.5+x}]O_4$ (x = 0, 0.05, and 0.08) Spinel Cathodes for Lithium-Ion Batteries. *Chem. Mater.* **2012**, *24* (15), 3101−3109.

(12) Jafta, C. J.; Mathe, M. K.; Manyala, N.; Roos, W. D.; Ozoemena, K. I. Microwave-Assisted Synthesis of High-Voltage Nanostructured $LiMn_{1.5}Ni_{0.5}O_4$ Spinel: Tuning the Mn^{3+} Content and Electrochemical Performance. *ACS Appl. Mater. Interfaces* **2013**, *5* (15), 7592−7598.

(13) Xiao, J.; Chen, X.; Sushko, P. V.; Sushko, M. L.; Kovarik, L.; Feng, J.; Deng, Z.; Zheng, J.; Graff, G. L.; Nie, Z.; Choi, D.; Liu, J.;

Zhang, J.-G.; Whittingham, M. S. High-Performance LiNi $_{0.5}$ Mn $_{1.5}$ O $_{4}$ Spinel Controlled by Mn $^{3+}$ Concentration and Site Disorder. *Adv. Mater.* **2012**, *24* (16), 2109−2116.
(14) Yi, T. F.; Mei, J.; Zhu, Y. R. Key Strategies for Enhancing the Cycling Stability and Rate Capacity of $LiNi_{0.5}Mn_{1.5}O_4$ as High-Voltage Cathode Materials for High Power Lithium-Ion Batteries. *J. Power Sources* **2016**, *316*, 85−105.
(15) Zheng, J.; Xiao, J.; Yu, X.; Kovarik, L.; Gu, M.; Omenya, F.; Chen, X.; Yang, X. Q.; Liu, J.; Graff, G. L.; Whittingham, M. S.; Zhang, J. G. Enhanced Li $^{+}$ Ion Transport in LiNi $_{0.5}$Mn $_{1.5}$O $_{4}$ through Control of Site Disorder. *Phys. Chem. Chem. Phys.* **2012**, *14* (39), 13515−13521.
(16) Cabana, J.; Casas-Cabanas, M.; Omenya, F. O.; Chernova, N. A.; Zeng, D.; Whittingham, M. S.; Grey, C. P. Composition-Structure Relationships in the Li-Ion Battery Electrode Material $LiNi_{0.5}Mn_{1.5}O_4$. *Chem. Mater.* **2012**, *24* (15), 2952−2964.
(17) Cabana, J.; Zheng, H.; Shukla, A. K.; Kim, C.; Battaglia, V. S.; Kunduraci, M. Comparison of the Performance of $LiNi_{1/2}Mn_{3/2}O_4$ with Different Microstructures. *J. Electrochem. Soc.* **2011**, *158* (9), A997.
(18) Lin, H. B.; Zhang, Y. M.; Rong, H. B.; Mai, S. W.; Hu, J. N.; Liao, Y. H.; Xing, L. D.; Xu, M. Q.; Li, X. P.; Li, W. S. Crystallographic Facet- and Size-Controllable Synthesis of Spinel LiNi $_{0.5}$Mn$_{1.5}$O$_4$ with Excellent Cyclic Stability as Cathode of High Voltage Lithium Ion Battery. *J. Mater. Chem. A* **2014**, *2* (30), 11987−11995.
(19) Cai, Y.; Huang, S. Z.; She, F. S.; Liu, J.; Zhang, R. L.; Huang, Z. H.; Wang, F. Y.; Wang, H. E. Facile Synthesis of Well-Shaped Spinel $LiNi_{0.5}Mn_{1.5}O_4$ Nanoparticles as Cathode Materials for Lithium Ion Batteries. *RSC Adv.* **2016**, *6* (4), 2785−2792.
(20) Xiao, J.; Chen, X.; Sushko, P. V.; Sushko, M. L.; Kovarik, L.; Feng, J.; Deng, Z.; Zheng, J.; Graff, G. L.; Nie, Z.; Choi, D.; Liu, J.; Zhang, J.-G.; Whittingham, M. S. High-Performance LiNi $_{0.5}$ Mn $_{1.5}$ O $_{4}$ Spinel Controlled by Mn $^{3+}$ Concentration and Site Disorder. *Adv. Mater.* **2012**, *24* (16), 2109−2116.
(21) Shu, Y.; Xie, Y.; Yan, W.; Meng, S.; Sun, D.; Jin, Y.; He, K. Synergistic Effect of Surface Plane and Particle Sizes on the Electrochemical Performance of $LiNi_{0.5}Mn_{1.5}O_4$ Cathode Material via a Facile Calcination Process. *J. Power Sources* **2019**, *433*, 226708.
(22) Liu, H.; Zhang, X.; He, X.; Senyshyn, A.; Wilken, A.; Zhou, D.; Fromm, O.; Niehoff, P.; Yan, B.; Li, J.; Muehlbauer, M.; Wang, J.; Schumacher, G.; Paillard, E.; Winter, M.; Li, J. Truncated Octahedral High-Voltage Spinel $LiNi_{0.5}Mn_{1.5}O_4$ Cathode Materials for Lithium Ion Batteries: Positive Influences of Ni/Mn Disordering and Oxygen Vacancies. *J. Electrochem. Soc.* **2018**, *165* (9), A1886−A1896.
(23) Casas-Cabanas, M.; Kim, C.; Rodríguez-Carvajal, J.; Cabana, J. Atomic Defects during Ordering Transitions in $LiNi_{0.5}Mn_{1.5}O_4$ and Their Relationship with Electrochemical Properties. *J. Mater. Chem. A* **2016**, *4* (21), 8255−8262.
(24) Duncan, H.; Hai, B.; Leskes, M.; Grey, C. P.; Chen, G. Relationships between Mn3+ Content, Structural Ordering, Phase Transformation, and Kinetic Properties in $LiNi_xMn_{2-X}O_4$ Cathode Materials. *Chem. Mater.* **2014**, *26* (18), 5374−5382.
(25) Kim, J. H.; Myung, S. T.; Sun, Y. K. Molten Salt Synthesis of $LiNi_{0.5}Mn_{1.5}O_4$ Spinel for 5 V Class Cathode Material of Li-Ion Secondary Battery. *Electrochim. Acta* **2004**, *49* (2), 219−227.
(26) Wen, L.; Lu, Q.; Xu, G. Molten Salt Synthesis of Spherical $LiNi_{0.5}Mn_{1.5}O_4$ Cathode Materials. *Electrochim. Acta* **2006**, *51* (21), 4388−4392.
(27) Börner, M.; Niehoff, P.; Vortmann, B.; Nowak, S.; Winter, M.; Schappacher, F. M. Comparison of Different Synthesis Methods for $LiNi_{0.5}Mn_{1.5}O_4$—Influence on Battery Cycling Performance, Degradation, and Aging. *Energy Technol.* **2016**, *4* (12), 1631−1640.
(28) Hai, B.; Shukla, A. K.; Duncan, H.; Chen, G. The Effect of Particle Surface Facets on the Kinetic Properties of $LiMn_{1.5}Ni_{0.5}O_4$ Cathode Materials. *J. Mater. Chem. A* **2013**, *1* (3), 759−769.
(29) Basin, A. S.; Kaplun, A. B.; Meshalkin, A. B.; Uvarov, N. F. The LiCl-KCl Binary System. *Russ. J. Inorg. Chem.* **2008**, *53* (9), 1509−1511.
(30) Qiao, R.; Wray, L. A.; Kim, J. H.; Pieczonka, N. P. W.; Harris, S. J.; Yang, W. Direct Experimental Probe of the Ni(II)/Ni(III)/Ni(IV) Redox Evolution in $LiNi_{0.5}Mn_{1.5}O_4$ Electrodes. *J. Phys. Chem. C* **2015**, *119* (49), 27228−27233.
(31) Kunduraci, M.; Al-Sharab, J. F.; Amatucci, G. G. High-Power Nanostructured LiMn $_{2-X}$Ni$_X$O$_4$ High-Voltage Lithium-Ion Battery Electrode Materials: Electrochemical Impact of Electronic Conductivity and Morphology. *Chem. Mater.* **2006**, *18* (15), 3585−3592.
(32) Sushko, P. V.; Rosso, K. M.; Zhang, J. G.; Liu, J.; Sushko, M. L. Oxygen Vacancies and Ordering of D-Levels Control Voltage Suppression in Oxide Cathodes: The Case of Spinel $LiNi_{0.5}Mn_{1.5}O_{4-\delta}$. *Adv. Funct. Mater.* **2013**, *23* (44), 5530−5535.
(33) Xue, Y.; Han, Y.; Wang, Z. B.; Zheng, L. L.; Yu, F.; Da; Zhou, Y. X. Study on $LixNi_{0.5}Mn_{1.5}O_4$ (x = 0.8, 0.9, 1, 1.1, and 1.2) High-Voltage Cathode for Lithium-Ion Batteries. *Ionics* **2018**, *24* (11), 3317−3323.
(34) Shannon, R. D. Revised Effective Ionic Radii and Systematic Studies of Interatomic Distances in Halides and Chalcogenides. *Acta Crystallogr., Sect. A: Cryst. Phys., Diffr., Theor. Gen. Crystallogr.* **1976**, *32* (5), 751−767.
(35) Lantelme, F.; Turq, P. Ionic Dynamics in the LiCl-KCl System at Liquid State. *J. Chem. Phys.* **1982**, *77* (6), 3177−3187.
(36) Amdouni, N.; Zaghib, K.; Gendron, F.; Mauger, A.; Julien, C. M. Structure and Insertion Properties of Disordered and Ordered LiNi $_{0.5}$Mn$_{1.5}$O$_4$ Spinels Prepared by Wet Chemistry. *Ionics* **2006**, *12* (2), 117−126.
(37) Lin, F.; Liu, Y.; Yu, X.; Cheng, L.; Singer, A.; Shpyrko, O. G.; Xin, H. L.; Tamura, N.; Tian, C.; Weng, T.-C.; Yang, X.-Q.; Meng, Y. S.; Nordlund, D.; Yang, W.; Doeff, M. M. Synchrotron X-Ray Analytical Techniques for Studying Materials Electrochemistry in Rechargeable Batteries. *Chem. Rev.* **2017**, *117* (21), 13123−13186.
(38) Suntivich, J.; Hong, W. T.; Lee, Y. L.; Rondinelli, J. M.; Yang, W.; Goodenough, J. B.; Dabrowski, B.; Freeland, J. W.; Shao-Horn, Y. Estimating Hybridization of Transition Metal and Oxygen States in Perovskites from o k -Edge X-Ray Absorption Spectroscopy. *J. Phys. Chem. C* **2014**, *118* (4), 1856−1863.
(39) De Groot, F. M. F.; Grioni, M.; Fuggle, J. C.; Ghijsen, J.; Sawatzky, G. A.; Petersen, H. Oxygen 1s X-Ray-Absorption Edges of Transition-Metal Oxides. *Phys. Rev. B: Condens. Matter Mater. Phys.* **1989**, *40* (8), 5715−5723.
(40) Vradman, L.; Zana, J.; Kirschner, A.; Herskowitz, M. Synthesis of $LaMnO_3$ in Molten Chlorides: Effect of Preparation Conditions. *Phys. Chem. Chem. Phys.* **2013**, *15* (26), 10914−10920.
(41) Susman, M. D.; Pham, H. N.; Zhao, X.; West, D. H.; Chinta, S.; Bollini, P.; Datye, A. K.; Rimer, J. D. Synthesis of NiO Crystals Exposing Stable High-Index Facets. *Angew. Chem.* **2020**, anie.202003390. DOI: 10.1002/ange.202003390
(42) Meir, R.; Vradman, L.; Zana, J.; Herskowitz, M. Effect of Salt Type on the Particle Size of $LaMn_{1-X}Fe_xO_3$ ($0.1 \leq x \leq 0.5$) Synthesized in Molten Chlorides. *Mater. Chem. Phys.* **2019**, *231*, 181−187.
(43) Chemelewski, K. R.; Li, W.; Gutierrez, A.; Manthiram, A. High-Voltage Spinel Cathodes for Lithium-Ion Batteries: Controlling the Growth of Preferred Crystallographic Planes through Cation Doping. *J. Mater. Chem. A* **2013**, *1* (48), 15334−15341.
(44) Chemelewski, K. R.; Shin, D. W.; Li, W.; Manthiram, A. Octahedral and Truncated High-Voltage Spinel Cathodes: The Role of Morphology and Surface Planes in Electrochemical Properties. *J. Mater. Chem. A* **2013**, *1* (10), 3347−3354.
(45) Yoon, K. H.; Cho, Y. S.; Kang, D. H. Molten Salt Synthesis of Lead-Based Relaxors. *J. Mater. Sci.* **1998**, *33*, 2977−2984.
(46) Yang, X.; Tang, W.; Kanoh, H.; Ooi, K. Synthesis of Lithium Manganese Oxide in Different Lithium-Containing Fluxes. *J. Mater. Chem.* **1999**, *9* (10), 2683−2690.
(47) Zhou, J.; Hong, D.; Wang, J.; Hu, Y.; Xie, X.; Fang, H. Electronic Structure Variation of the Surface and Bulk of a LiNi $_{0.5}$Mn$_{1.5}$O$_4$ Cathode as a Function of State of Charge: X-Ray Absorption Spectroscopic Study. *Phys. Chem. Chem. Phys.* **2014**, *16* (27), 13838−13842.

https://dx.doi.org/10.1021/acs.inorgchem.0c01042
Inorg. Chem. XXXX, XXX, XXX−XXX

(48) Xue, Y.; Han, Y.; Yu, H. X.; Shu, J.; Wang, Z. B.; Zheng, L. L.; Xia, Y. F. Improving Rate Performance of High-Voltage Spinel Cathode by Changing Structural Evolution from Two-Phase to Solid-Solution Reactions. *Electrochim. Acta* **2018**, *281*, 24−30.
(49) Han, Y.; Xue, Y.; Xia, Y. F.; Zhang, J. N.; Yu, F. Da; Gu, D. M.; Wang, Z. B. Design of Synergistic-Coated Layer of La_2O_3/Al_2O_3 in $LiNi_{0.5}Mn_{1.5}O_4$ Cathode for Enhanced Cycling Stability and Rate Capability. *Ionics* **2019**, *25* (6), 2459−2468.
(50) Liu, H.; Wang, J.; Zhang, X.; Zhou, D.; Qi, X.; Qiu, B.; Fang, J.; Kloepsch, R.; Schumacher, G.; Liu, Z.; Li, J. Morphological Evolution of High-Voltage Spinel $LiNi_{0.5}Mn_{1.5}O_4$ Cathode Materials for Lithium-Ion Batteries: The Critical Effects of Surface Orientations and Particle Size. *ACS Appl. Mater. Interfaces* **2016**, *8* (7), 4661−4675.
(51) Zhou, M.; Gong, J.; Deng, Z.; Lang, Y.; Zong, B.; Guo, J.; Wang, L. Synthesis and Electrochemical Performances of $LiNi_{0.5}Mn_{1.5}O_4$ Spinels with Different Surface Orientations for Lithium-Ion Batteries. *Ionics* **2020**, *26*, 2187−2200.
(52) Yang, J.; Han, X.; Zhang, X.; Cheng, F.; Chen, J. Spinel $LiNi_{0.5}Mn_{1.5}O_4$ cathode for Rechargeable Lithiumion Batteries: Nano vs Micro, Ordered Phase ($P4_332$) vs Disordered Phase ($Fd\bar{3}m$). *Nano Res.* **2013**, *6* (9), 679−687.

https://dx.doi.org/10.1021/acs.inorgchem.0c01042
Inorg. Chem. XXXX, XXX, XXX−XXX